Sensitive CO and ^{13}CO survey of water fountain stars.

Detections towards IRAS 18460-0151 and IRAS 18596+0315

J. R. Rizzo[1], J. F. Gómez[2], L. F. Miranda[3, 4], M. Osorio[2], O. Suárez[5], and M. C. Durán-Rojas[2]

[1] Centro de Astrobiología (INTA-CSIC), Ctra. M-108, km. 4, E-28850 Torrejón de Ardoz, Spain
e-mail: `ricardo@cab.inta-csic.es`
[2] Instituto de Astrofísica de Andalucía (CSIC), Apartado 3004, E-18080 Granada, Spain
[3] Consejo Superior de Investigaciones Científicas, Serrano 117, E-28006 Madrid, Spain
[4] Departamento de Física Aplicada, Universidade de Vigo, Campus Lagoas-Marcosende s/n, E-36310 Vigo, Spain
[5] UMR 6525 H.Fizeau, Université de Nice Sophia Antipolis, CNRS, OCA. Parc Valrose, F-06108 Nice Cedex 2, France

ABSTRACT

Context. Water fountain stars represent a stage between the asymptotic giant branch (AGB) and planetary nebulae phases, when the mass loss changes from spherical to bipolar. These types of evolved objects are characterized by high-velocity jets in the 22 GHz water maser emission.

Aims. The objective of this work is to detect and study in detail the circumstellar gas in which the bipolar outflows are emerging. The detection and study of thermal lines may help in understanding the nature and physics of the envelopes in which the jets are developing.

Methods. We surveyed the CO and ^{13}CO line emission towards a sample of ten water fountain stars through observing the $J = 1 \rightarrow 0$ and $2 \rightarrow 1$ lines of CO and ^{13}CO, using the 30 m IRAM radio telescope at Pico Veleta. All the water fountains visible from the observatory were surveyed.

Results. Most of the line emission arises from foreground or background Galactic clouds, and we had to thoroughly analyse the spectra to unveil the velocity components related to the stars. In two sources, IRAS 18460-0151 and IRAS 18596+0315, we identified wide velocity components with a width of $35 - 40$ km s^{-1} that are centred at the stellar velocities. These wide components can be associated with the former AGB envelope of the progenitor star. A third case, IRAS 18286-0959, is reported as tentative; in this case a pair of narrow velocity components, symmetrically located with respect to the stellar velocity, has been discovered. We also modelled the line emission using an LVG code and derived some global physical parameters, which allowed us to discuss the possible origin of this gas in relation to the known bipolar outflows. For IRAS 18460-0151 and IRAS 18596+0315, we derived molecular masses close to $0.2\,M_\odot$, mean densities of 10^4 cm^{-3}, and mass-loss rates of $10^{-4}\,M_\odot$ yr^{-1}. The kinetic temperatures are rather low, between 10 and 50 K in both cases, which suggests that the CO emission is arising from the outer and cooler regions of the envelopes. No fitting was possible for IRAS 18286-0959, because line contamination can not be discarded in this case.

Conclusions. The molecular masses, mean densities, and mass-loss rates estimated for the circumstellar material associated with IRAS 18460-0151 and IRAS 18596+0315 confirm that these sources are at the end of the AGB or the beginning of the post-AGB evolutionary stages. The computed mass-loss rates are among the highest ones possible according to current evolutionary models, which leads us to propose that the progenitors of these water fountains had masses in the range from 4 to 8 $M_\odot$. We speculate that CO emission is detected in water fountains as a result of a CO abundance enhancement caused by current episodes of low-collimation mass-loss.

Key words. masers – stars: AGB and post-AGB – stars: evolution – stars: individual (IRAS 18460-0151, IRAS 18596+0315, IRAS 18286-0959) – stars: winds, outflows – ISM: molecules

1. Introduction

Planetary nebulae (PNe) display a variety of morphologies, from purely spherical (see, e.g., Jacoby et al. 2010) to bipolar or even multipolar (Sahai & Trauger 1998). Non-spherical PNe are of particular interest, because the explanation of the process that shapes them is still under debate. There is growing evidence of highly collimated jets in evolved stars, which are believed to play a key role in the subsequent shaping of PNe (Sahai & Trauger 1998). For low- and intermediate-mass stars ($0.8-8\,M_\odot$), a short-lived transition from a spherical to a collimated mass-loss at some point between the asymptotic giant branch (AGB) and the PNe stages is therefore expected. Several processes have been proposed to explain the nature of collimated ejections in these

evolved stars, such as the magnetic launching from a single star (García-Segura et al. 2005) or a binary system (Soker 1998).

A crucial step in this study is identifying the sources that have just made the transition from spherical to collimated mass-loss. The group of objects often referred to as water fountain stars (hereafter WF) are probably the most appropriate candidates. WFs are evolved objects (mostly late AGB and post-AGB stars) with water maser emission tracing high-velocity motions, faster than the typical velocities seen in AGB mass-loss motions of $10 - 30$ km s^{-1} (see, for example, Neri et al. 1998). Candidate objects to this class are usually identified by their broad velocity spread ($\gtrsim 50$ km s^{-1}) in their water maser spectra. Since the first identification of IRAS 16342-3814 (Likkel & Morris 1988), this novel group of sources has grown very little in num-

ber. A total of only 14 candidate WFs have been reported so far (Engels et al. 1986; Deacon et al. 2007; Deguchi et al. 2007; Suárez et al. 2008, 2009; Day et al. 2010; Gómez et al. 2011).

When water maser emission in WFs is observed with interferometers, it seems to trace highly collimated jets, with dynamical ages as young as < 100 yr (Boboltz & Marvel 2007; Imai 2007a; Day et al. 2010). In IRAS 18286-0959, the water masers are tracing a double-helix structure (Yung et al. 2011). In all cases, these recent ejections represent one of the earliest known manifestations of collimated mass-loss in evolved stars.

WFs are thought to possess a thick, expanding circumstellar envelope (CSE), that was expelled during the AGB phase. The maser emission in these sources may be produced when a newly produced jet strikes into the CSE (Imai 2007a). This scenario explains the highly collimated jets of OH and H_2O with velocities higher than $100 \, km \, s^{-1}$ (Boboltz & Marvel 2007; Day et al. 2010; Gómez et al. 2011) and very short dynamical time-scales. After some decades, the tip of the jet is expected to have reached the outer regions of the CSE, where physical conditions for maser pumping are no longer met. The thick CSE in WF is evident by their high obscuration in optical wavelengths.

The modelling of the broad-band spectral energy distribution (SED) of the thermal dust emission may give important clues about the envelope in WFs and also about the presence of disks (Durán-Rojas et al., in preparation). SED modelling may, in principle, provide hints about the circumstellar mass, the luminosity of the system (e.g., including both the envelope and the disk), and the physical structure (density and temperature profiles). Unfortunately, SED modelling is still hampered by some free parameters that are poorly constrained due to the complexity of the sources (star, envelope, disks, jets) and the lack of knowledge of some global parameters.

The detection and detailed study of line emission from thermal gas is a key in providing additional valuable information about the physical characteristics of CSEs, mainly about the total mass, the mass-loss rate and the global kinematics. CO and ^{13}CO spectra have been widely observed in AGB and post-AGB stars; modelling them has been used to determine the mass-loss rate, the total mass, and other physical parameters (see, for example, Teyssier et al. 2006). So far, IRAS 16342-3814 is the only WF where thermal line emission has been unambiguously reported (He et al. 2008; Imai et al. 2009). From the detection of the CO and (tentatively) ^{13}CO $J = 2 \rightarrow 1$ lines, He et al. (2008) have determined an expansion velocity of $46 \, km \, s^{-1}$, higher than that expected in an AGB envelope (typically $15 \, km \, s^{-1}$). Surprisingly, the CO $J = 3 \rightarrow 2$ line reported recently (Imai et al. 2012) shows a different kinematics, depicting an even broader profile ($> 200 \, km \, s^{-1}$). These high-velocity dispersions have been interpreted by the kinematics related to the collimated ejection also traced by water masers, instead of with the expanding motions of the CSE.

Imai et al. (2009) illustrated the difficulty of properly identifying CO associated with WFs when using single-dish observations. Most of these objects are at low Galactic latitude and therefore multiple Galactic foreground and background CO components are also gathered within the telescope beam. It is necessary to take spectra offset from the target position, and identify whether there are CO components that are present only at the target position, and at a velocity close to that of the star. Imai et al. (2009) reported a tentative detection of CO $J = 3 \rightarrow 2$ emission associated with IRAS 18286-0959, since it was only present in spectra taken towards this source. However, its large velocity offset ($\simeq 25 \, km \, s^{-1}$) from the central velocity of the jet and the

narrow width of the line precluded these authors to ascertain the association of the CO emission with the WF.

We conducted sensitive CO and ^{13}CO observations of ten WFs, involving the $J = 1 \rightarrow 0$ and $2 \rightarrow 1$ transitions, using the 30m IRAM radio telescope at Pico Veleta. Our goal was to survey the largest possible number of WFs to obtain new reliable detections of thermal line emission associated with these objects, and hence to derive some global physical parameters of the emitting regions.

2. Observations and strategy

The observations were carried out using the 30 m radio telescope at Pico Veleta, Spain, during two runs in June 2009 and June 2010. The new EMIR (Eight MIxer Receiver) was used for all the observations. The focal plane geometry of this instrument allowed us to gather 3 mm and 1 mm data simultaneously in two linear polarizations. In this case, we selected the simultaneous observations of CO $J = 1 \rightarrow 0$ (115.271 GHz) and $J = 2 \rightarrow 1$ (230.538 GHz) in one receiver configuration, and ^{13}CO $J = 1 \rightarrow 0$ (110.201 GHz) and $J = 2 \rightarrow 1$ (220.399 GHz) in a second setup.

Both the VESPA and WILMA autocorrelators were connected as backends at all the observed lines. With VESPA, a frequency spacing of 312 kHz and 1.25 MHz was employed in the 3 mm and 1 mm lines. This is equivalent to 0.81 and $0.85 \, km \, s^{-1}$ at the CO and ^{13}CO $J = 1 \rightarrow 0$ frequencies; at the $J = 2 \rightarrow 1$ lines, the velocity spacings are twice as high. The theoretical bandwidth employed was 160 MHz and 320 MHz at 3 mm and 1 mm, which provided an actual velocity coverage of $\sim 360 \, km \, s^{-1}$ in all the lines. On the other hand, each module of the WILMA autocorrelator provided 1 GHz of bandwidth and a fixed spectral resolution of 2 MHz. The wide instantaneous bandwidth of EMIR (8 GHz in SSB at 3 mm) allowed us to tune the local oscillator to include the ^{13}CO $J = 1 \rightarrow 0$ line in the CO setup. Therefore, we used another WILMA module to cross-check the ^{13}CO $J = 1 \rightarrow 0$ line emission within the CO setup, albeit with a poor velocity resolution ($5.4 \, km \, s^{-1}$).

The observations were made under typical winter conditions (precipitable water vapour column close to 4 mm), registering atmospheric opacities at 225 GHz between 0.1 and 0.4. Typical system temperatures were 110–450 K at 3 mm, and 160–600 K at 1 mm. The resulting *rms* (three-sigma) were between 8 mK and 92 mK at 3 mm, and between 26 mK and 250 mK at 1 mm.

The antenna temperature scale was calibrated every 10–12 minutes by the standard chopper wheel method, that is, by the sequential observation of hot and cold loads, and the blank sky; hot and cold load temperatures were room- and liquid-nitrogen temperatures, respectively. Sky attenuation was determined in real time from the values of a weather station, the measurement of the sky emissivity, and an atmosphere numerical model available at the observatory. Furthermore, we regularly observed a set of standard line calibrators (Mauersberger et al. 1989), and estimated an uncertainty lower than 20% in all the observed lines.

All the intensities throughout the paper are made with respect to a scale of main-beam temperature (T_{MB}), assuming main-beam efficiencies of 0.75 and 0.52 at 3 mm and 1 mm. Velocities are given with respect to the LSR.

We surveyed all the WFs known in 2010 that are visible from Pico Veleta. The sample includes ten sources, detailed in Table 1. In the table we included other common names for the sources, their equatorial coordinates (J2000), distances, Galactic latitudes, and approximate velocities with respect to the LSR. The two distances quoted for IRAS 18113-2503 are kinematic

Table 1. Sources observed

IRAS name	Other name	RA	Dec	d	b	V_{LSR}	Ref.
		J2000		kpc	deg	km s^{-1}	
16552-3050	GLMP 498	16:58:27.30	−30:55:08.0	19.6	+7.3	+20	1,2
18043-2116	OH0.9-0.4	18:07:20.86	−21:16:10.9	6.4	−0.4	+90	3
18113-2503		18:14:27.27	−25:03:00.5	6.7 or 10.0	−3.6	+100	4
18139-1816?	**OH12.8-0.9**	18:16:49.23	−18:15:01.8	—	−0.9	+60	5,6
18286-0959		18:31:22.95	−09:57:21.1	3.6	−0.1	+41	7,8
18450-0148	**W43A**	18:47:41.16	−01:45:11.5	2.6	0.0	+34	9,10
18460-0151	OH31.0-0.2	18:48:43.02	−01:48:30.5	2.1	−0.2	+125	11,12
18596+0315	OH37.1-0.8	19:02:06.26	+03:20:15.5	4.6 or 8.8	−0.8	+90	13
19134+2131		19:15:35.22	+21:36:33.9	8.0	+4.6	−65	14
19190+1102		19:21:25.09	+11:08:41.0	8.6	−1.5	+20	15

References. (1) Suárez et al. (2007); (2) Suárez et al. (2008); (3) Deacon et al. (2007); (4) Gómez et al. (2011); (5) Engels et al. (1986); (6) Boboltz & Marvel (2005); (7) Imai et al. (2013a); (8) Yung et al. (2011); (9) Diamond et al. (1985); (10) Imai et al. (2005); (11) Deguchi et al. (2007); (12) Imai et al. (2013b); (13) Gómez et al. (1994); (14) Imai et al. (2007b); (15) Day et al. (2010).

Notes. In boldface are given the most common name and that used throughout this paper.
Unclear association of IRAS 18139-1816 to OH12.8-0.9, probably due to wrong coordinates in the IRAS catalogue.
Kinematic distances provided for IRAS 18113-2503 (see text).
Unknown distance to OH12.8-0.9. Baud et al. (1985) proposed 8 kpc due to its membership to a group of evolved stars located towards the Galactic Center.

distances derived in this work, using the Galactic rotation model of Reid et al. (2009).

All the observed sources are located in the Galactic disk, and most of them at Galactic latitudes as low as $|b| < 1°$. Therefore, the CO and ^{13}CO lines are expected to be heavily contaminated by Galactic background or foreground emission that originates in local gas and spiral arm clouds along the line of sight.

Therefore, we selected position-switching as the observing mode and were especially careful in selecting an appropriate reference position. For each source, we tried different reference positions by moving away from the Galactic plane, until we obtained clean spectra, that is, without line emission arising from the reference position.

However, a position used for reference that is too distant usually produces a worsening in the baselines, and we had to compromise. Typical distances to the reference positions were 1000″.

To associate a velocity component to a WF, we proceeded with a strategy of five-points crosses, that is, by observing towards the star position, and another four points located 24″ away from it, in the east-west and north-south directions. This separation of 24″ corresponds approximately to the half-power beam width (HPBW) at 3 mm, and twice the HPBW at 1 mm. Due to galactic foreground/background gas clumps, one can expect significant variations in the emission along 24″. However, if we saw a velocity component present ONLY at the star position, this was suspected to be associated to the WF, and was analysed in detail.

When a WF source had no CO emission at the star position or only a narrow component far away from the stellar velocity, it was excluded from the five-points strategy. Because of time restrictions, we were unable to observe the ^{13}CO setup in IRAS 16552-3050 and OH12.8-0.9; in these sources, we were only able to use the $J = 1 \rightarrow 0$ spectra from WILMA, which were observed simultaneously with the ^{12}CO setup (as explained above).

Data reduction and analysis were made using the GILDAS software[1].

---

[1] GILDAS is a radio astronomy software developed by IRAM. See http://www.iram.fr/IRAMFR/GILDAS/.

Table 2. Upper limits of the undetected sources

IRAS name	CO		^{13}CO	
	$1 \rightarrow 0$	$2 \rightarrow 1$	$1 \rightarrow 0$	$2 \rightarrow 1$
16552-3050	0.83	0.64	0.36	—
18113-2503	1.08	2.15	0.25	0.27
19134+2131	0.61	0.72	0.53	1.61

**Notes.** Three-sigma *rms* limits in K km s^{-1}. Velocity width of 40 km s^{-1} assumed.

3. Results

3.1. Overview

In Figs. 1 to 4 the spectra towards the star position are depicted, corresponding to CO $J = 1 \rightarrow 0$, ^{13}CO $J = 1 \rightarrow 0$, CO $J = 2 \rightarrow 1$, and ^{13}CO $J = 2 \rightarrow 1$. In all cases but the ^{13}CO $J = 1 \rightarrow 0$ line of IRAS 16552-3050 and OH12.8-0.9 (Fig. 2), spectra are taken from the VESPA autocorrelator; for non-detections, a smoothing of three channels was applied to the spectra. Line emission, with multiple velocity components, is present in most of the spectra, but it mainly arises in foreground and background Galactic clouds. Notable exceptions are IRAS 16552-3050, IRAS 18113-2503 (both without CO emission), and IRAS 19134+2131 (with only a narrow component), which are the sources with the highest Galactic latitude in our sample. Table 2 provides the upper limits of the CO and ^{13}CO velocity-integrated temperatures in these cases, assuming a line width of 40 km s^{-1}.

The foreground and background molecular emission makes it difficult to ascertain the presence of emission associated with our target sources. Therefore, special care must be taken in finding this association. We propose a set of three requirements that a particular velocity component must fulfil for it to be considered as probably associated with the WFs: (1) it is present *only* at the star position; (2) it persists at least in two of the observed lines; and (3) it is centred as closely as possible at the stellar velocity.

These three criteria are independent of any additional interpretation of the geometry and kinematics of the CO-emitting region in WFs, and we consider them as indispensable require-
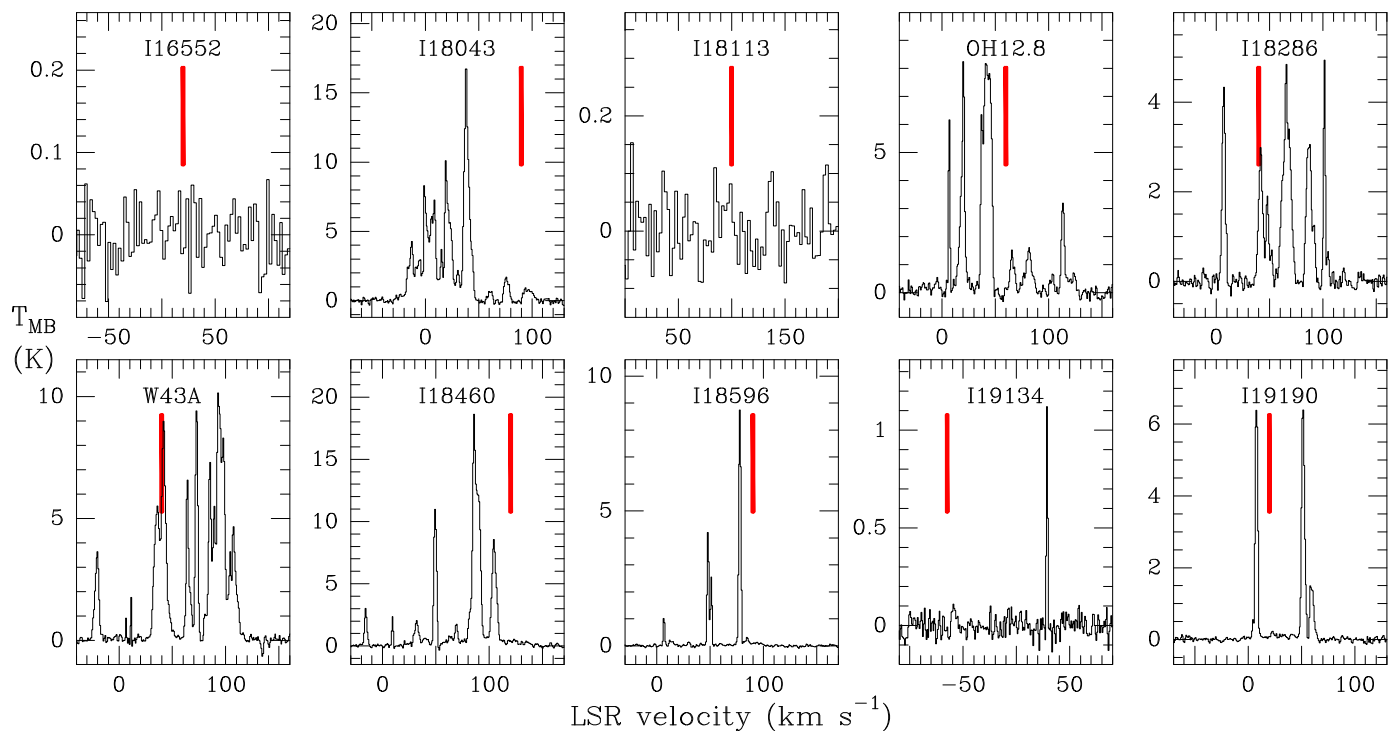
Fig. 1. CO $J = 1 \rightarrow 0$ spectra towards the ten WFs surveyed. The (shortened) source name is indicated at the top of each spectrum. Note the different intensity ranges in the panels. All the spectra span 200 km s^{-1} of coverage to facilitate line width comparisons among the sources. Spectra corresponding to IRAS 16552-3050 and IRAS 18113-2503 have been smoothed to three times the original velocity spacing. Red vertical bars are located at approximately the stellar velocity to facilitate additional association. Most of these velocity components arise from background or foreground Galactic clouds, as discussed in the text.

ments. In addition to these considerations, another reliability restriction can be imposed if we assume that CO emission arises in an expanding circumstellar shell, or in the region where this shell interacts with the stellar jet, or even in the inner disk. Therefore, we expect lines to have widths consistent with expanding motions found in AGB envelopes, or larger ($\simeq 15$ km s^{-1}).

After a thorough analysis of the five-points pattern of all sources and all emission lines, we identified two strong candidates that might possess thermal gas associated with them: IRAS 18460-0151 and IRAS 18596+0315; as we see in the next section, broad components are detected towards these sources. In a third case, IRAS 18286-0959, we discovered a pair of narrow CO velocity components, symmetrically located with respect to the mean OH and H$_2$O maser velocities (Sevenster et al. 1997; Imai et al. 2013a). While this source does not meet the three detection criteria we imposed, we cannot discard that the CO emission is associated with this WF, although with circumstellar characteristics different from those of the other two detections. We therefore include this source as a possible (albeit very tentative) detection in the following discussion.

3.2. Individual sources

3.2.1. IRAS 18460-0151

This is the clearest detection reported in this work and, if confirmed, would be the second WF known to show associated thermal line emission, after IRAS 16342-3814 (He et al. 2008; Imai et al. 2009, 2012). Figure 5 depicts all the final spectra towards this source; for each of the observed lines, a cross of panels shows the spectra at the five positions observed. To facilitate the identification of the associated feature, a zoom in intensity and velocity was applied.

A component of about 40 km s^{-1} width was detected *in the four lines* observed, and *only* towards the star position. In addition, this component is centred close to the stellar velocity, inferred from the double-peaked OH spectrum (te Lintel Hekkert et al. 1989; Engels & Jiménez-Esteban 2007) and also the H$_2$O emission (Deguchi et al. 2007). To emphasize the feature, the velocity range (115, 145) km s^{-1} has been shaded in the figure. This is the only velocity range where the above mentioned characteristics are found for this source.

The contrast between the star and the off-source positions is more notable in the two $J = 2 \rightarrow 1$ lines. In contrast, the ^{13}CO $J = 1 \rightarrow 0$ line shows a velocity component significantly narrower than the other lines.

The line ratio of CO (2-1)/(1-0) is higher than 2. This is an unusually high value for extended insterstellar clouds (see, e.g., Sakamoto et al. 1995), but it is more typical of a compact, unresolved source, which reinforces the association of this component to the CSE of the WF. The CO(2-1)/^{13}CO(2-1) ratio is remarkably low (between 2 and 3). This is also uncommon for an interstellar cloud, but similar values have been found in the WF IRAS 16342-3814 (He et al. 2008; Imai et al. 2012) and some AGB and post-AGB envelopes (see, for example, Bujarrabal et al. 2001, 2005; Teyssier et al. 2006). This point is discussed in Sect. 4, where we analyse the emission and estimates of physical parameters.

3.2.2. IRAS 18596+0315

This case is quite similar to IRAS 18460-0151, although the associated CO and ^{13}CO components are weaker than those of that source. Figure 6 displays all the final spectra for this source, sim-
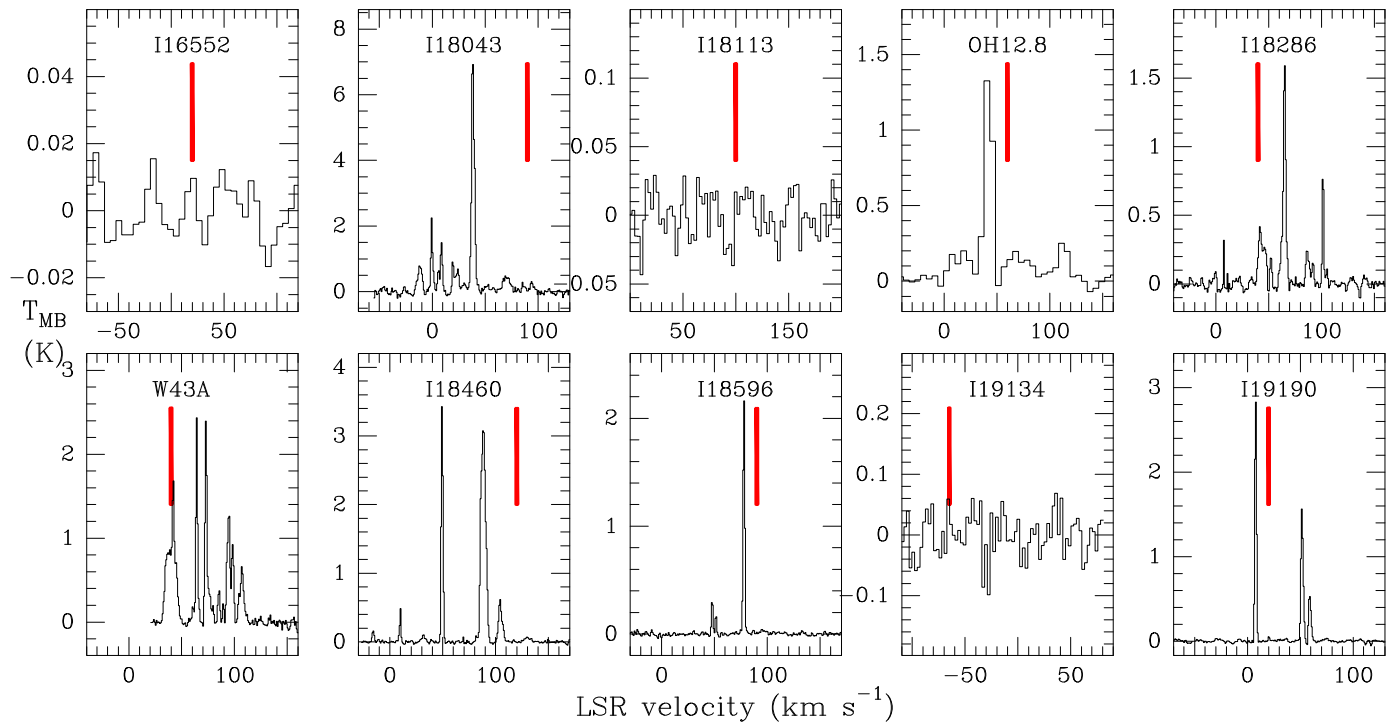
Fig. 2. Same as Fig. 1 for the ^{13}CO $J = 1 \rightarrow 0$ line. Spectra from IRAS 16552-3050 and OH12.8-0.9 correspond to the WILMA autocorrelator. Spectra corresponding to IRAS 18113-2503 and IRAS 19134+2131 have been smoothed to three times the original velocity spacing.
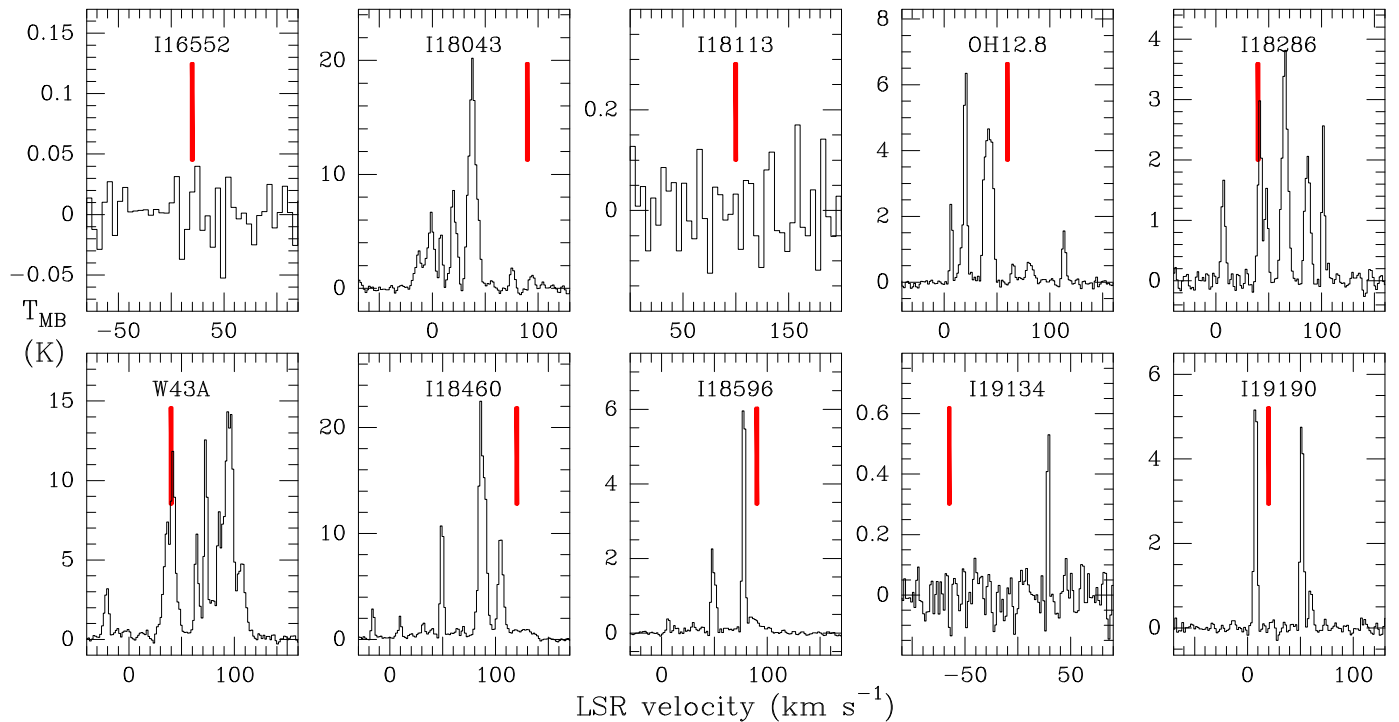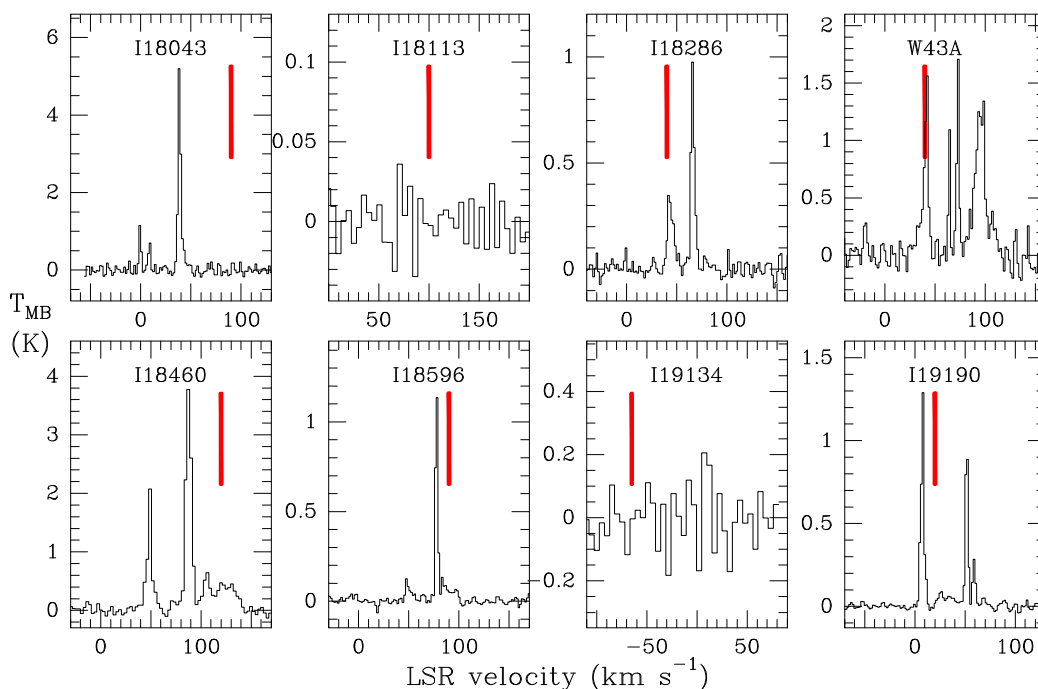

Fig. 3. Same as Figs. 1 and 2 for the CO $J = 2 \rightarrow 1$ line. Spectra corresponding to IRAS 16552-3050 and IRAS 18113-2503 have been smoothed to three times the original velocity spacing.

ilar to the previous figure. Again, a zoom in intensity and velocity was applied to emphasize the feature of interest.

In the velocity range (90, 105) km s^{-1} (shaded in the figure), there is significant emission only towards the source, and none elsewhere. As in the previous case, this is noted in all the spectral lines observed in the survey. The whole range of emission of this feature is indeed wider, as we show in the discussion. As in IRAS 18460-0151, the ^{13}CO $J = 1 \rightarrow 0$ line is the less evident, while the two $J = 2 \rightarrow 1$ lines are the clearest.

The line ratio of CO (2-1)/(1-0) is unusually high (around 2), as in IRAS 18460-0151. The CO/^{13}CO observed ratios are not as low as in IRAS 18460-0151; they vary between 3 and 5, depending on the $J \rightarrow (J-1)$ used for the computation. The implications of this difference is also discussed below.

Fig. 4. Same as Figs. 1–3 for the ^{13}CO $J = 2 \rightarrow 1$ line. The sources IRAS 16552-3050 and OH 12.8-0.9 have not been observed in this transition. Spectra corresponding to IRAS 18113-2503 and IRAS 19134+2131 have been smoothed to three times the original velocity spacing.

3.2.3. IRAS 18286-0959

This case is clearly different from the previous ones, because we did not find a wide velocity component. However, we did detect a pair of narrow lines, symmetrically located with respect to the stellar velocity. Figure 7 depicts all the final spectra towards this source, similar to Figs. 5 and 6. Unfortunately, we dealt with strong contamination in the offset positions of the two ^{13}CO lines at one of the velocity ranges of interest. For this reason, Fig. 7 contains only the CO lines at the five positions observed.

As was previously pointed out by Imai et al. (2009), the CO spectrum of IRAS 18286-0959 is rich in narrow components, due surely to its location in the Galactic plane. Nonetheless, two of these narrow components are particularly intense towards the star position and are weaker elsewhere. These two components lie at ~ 7 km s^{-1} and 66 km s^{-1}, and are partly shaded in the Fig. 7 to facilitate comparison of the intensities among the five positions. The association of these narrow components to the WF is very tentative, but worth analyzing to the extent that these data allow (see also the discussion by Imai et al. 2009).

Stellar velocities inferred from maser lines –due to their own nature and circumstellar origin– may have large uncertainties of up to 20 km s^{-1} (te Lintel Hekkert et al. 1989). Even taking into account this potentially large uncertainty, the mean velocities of the OH and H_2O masers are probably not far from the stellar velocity, and the CO mean velocity is also close to it. Another important factor is that the line profile is contaminated by the contribution of foreground and background clouds, especially the blueshifted component.

Imai et al. (2009) (their Fig. 2c) detected three velocity components in the CO $J = 3 \rightarrow 2$ line towards the star position, after subtracting the contribution of the off-source positions; the approximate velocities of these components are 10 km s^{-1}, 40 km s^{-1}, and 65 km s^{-1}. In our data, the 40 km s^{-1} component is not particularly intense at the star position, being noted only in the $J = 2 \rightarrow 1$ line.

In the other two components, the observed (2-1)/(1-0) line ratio is lower than one. As we discuss below, this difference with respect to IRAS 18460-0151 and IRAS 18596+0315 is a signature of different physical and excitation conditions.

4. Analysis and discussion

4.1. Possible origin of the detected CO

To analyse and characterize the molecular gas associated with the three WFs that may show circumstellar CO emission, we isolated the intrinsic CO velocity components by subtracting synthesized off-source spectra (obtained, in turn, as the average of the four outer spectra of each source). The results are presented in Fig. 8 for the three sources and for all the observed lines.

The wide component found in IRAS 18460-0151 and IRAS 18596+0315 strongly resembles those of the circumstellar envelopes found in different stages of late-type stars, such as planetary nebulae (see, for instance, Bujarrabal et al. 2005) and post-AGB stars (Bujarrabal et al. 2001; Teyssier et al. 2006). Wide components of 30–40 km s^{-1} are commonly associated with the previous AGB envelopes of these objects.

In the case of IRAS 18286-0959 the velocity components are narrower than in the other two cases, and the emission (if it is associated with the source) probably arises from a smaller, more concentrated region; there are also some examples of circumstellar envelopes that show this double-peaked profile, although –to the best of our knowledge– in C-rich evolved stars only (Yamamura et al. 1993; Bujarrabal & Cernicharo 1994). By increasing the degree of speculation, we can explore whether the CO arises from a thin dense shell that surrounds a bipolar cavity, as in the model of IRAS 16342-3814 made by Imai et al. (2012). The water jets recently studied by Yung et al. (2011) are organized in a double-helix structure, which may produce a pair of symmetric bullets, which are detected in CO.

The weaknesses of the lines (except IRAS 18286-0959), the unresolved nature of the emission, and the lack of detailed in-
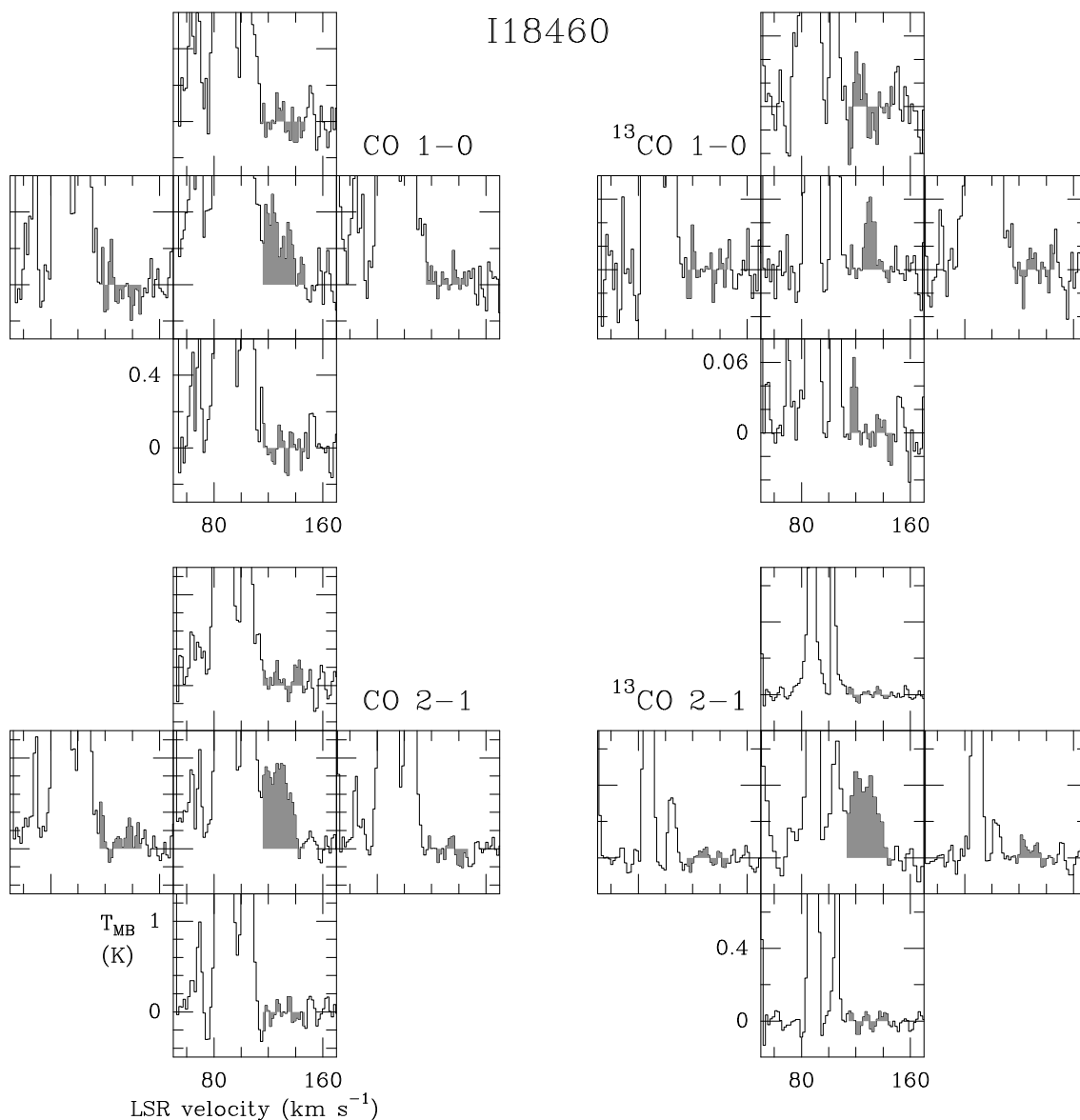
Fig. 5. All spectra observed towards IRAS 18460+0151. Each cross of five spectra corresponds to one of the CO lines. The relative locations of the spectra indicate the relative positions of antenna pointings; the centre towards the WF and four offset positions, 24″ away from the WF. The lines are indicated on top of each cross. The velocity range from 115 to 145 km s^{-1} has been shaded to facilitate additional comparison. As discussed in the text, this velocity range depicts significant emission only at the star position.

formation about the geometry and physics of the envelopes prevent a more detailed modelling. Nonetheless, first-order approximations were made by fitting the spectra. The shell method available in GILDAS was employed for IRAS 18460-0151 and IRAS 18596+0315. This method fits horn-type profiles for circumstellar envelopes, providing as outputs (1) the area of the spectrum; (2) $V_{\rm pk}$, the central velocity; (3) the expansion velocity ($V_{\rm exp}$), deduced from the full width at zero-level; and (5) s_τ, a shape parameter that is measured as the horn-to-centre ratio, which depends on the line opacity and takes values from -1 (for optically thick lines, parabolic shape) to infinity (for double-peaked, optically thin lines); values close to zero are interpreted as optically thin, flat-topped lines. The method assumes uniform physical conditions and does not take into account possible asymmetries due to excitation or clumping. For IRAS 18286-0959, this fitting method did not converge and we performed Gaussian fitting of the two components independently.

Table 3 shows the results of the fitting, and the thick red lines of Fig. 8 plot them superposed on the observed spectra. The fittings are sufficient as a first approximation. The mean velocities agree very well with the assumed systemic stellar velocity deduced from the masers. In IRAS 18460-0151 and IRAS 18596+0315, the two CO lines and the $J = 2 \rightarrow 1$ line of ^{13}CO are optically thick, while the $J = 1 \rightarrow 0$ line of ^{13}CO is optically thin in both sources. In any case, the fitting for the last line is the least reliable of all, particularly for IRAS 18596+0315. Some hints of possible asymmetries are also noted and are worth to be studied in detail during follow-up observations.

Average expansion velocities (weighted by the inverse square of the errors) are 20.1 km s^{-1} and 17.7 km s^{-1} for IRAS 18460-0151 and IRAS 18596+0315. These velocities are consistent with an AGB origin of the molecular gas, as mentioned before.

From Table 3 we can also quantify some important line ratios. The CO and ^{13}CO $(2 - 1)/(1 - 0)$ ratio varies between 2
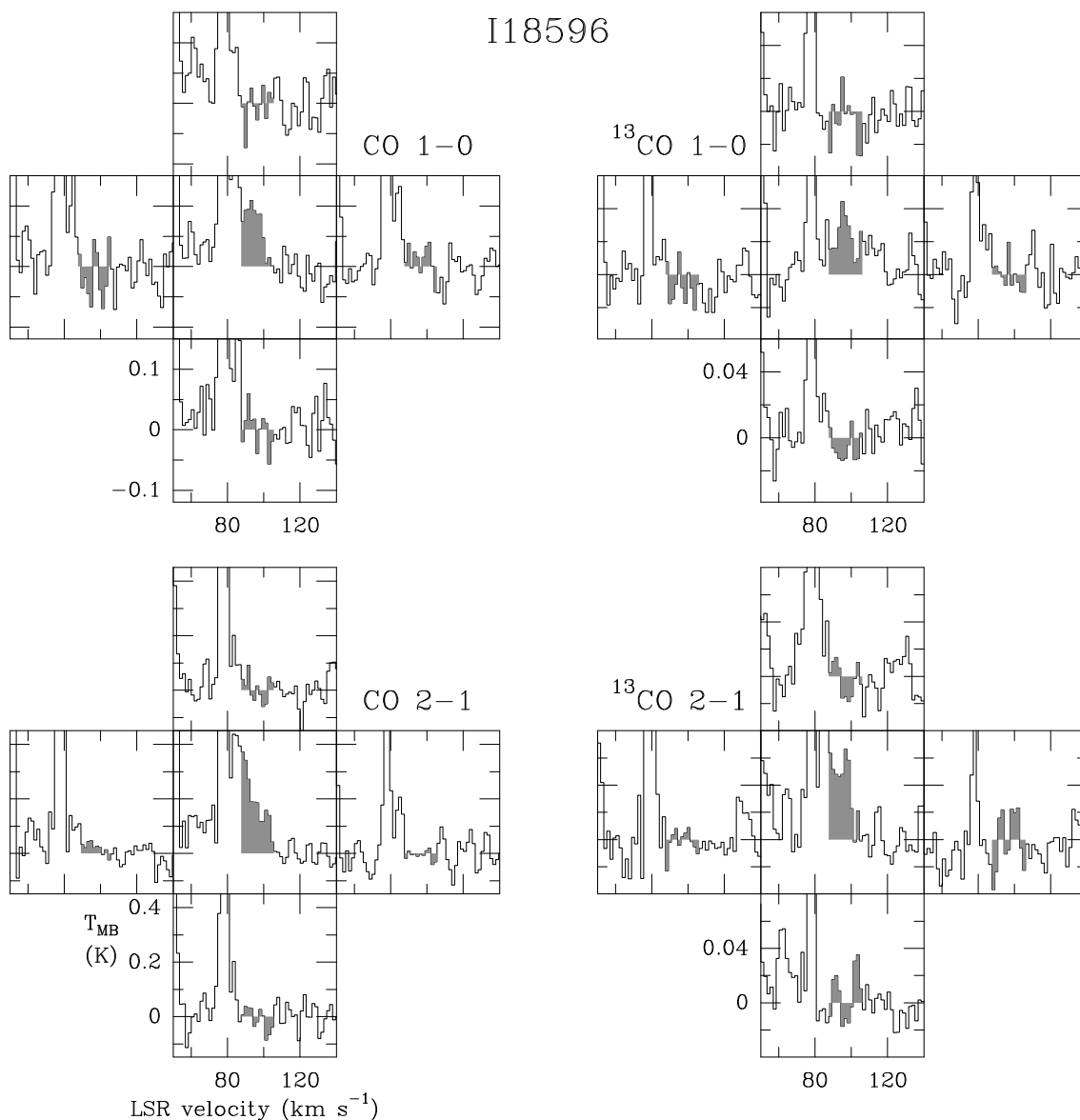
Fig. 6. Same as Fig. 5 for IRAS 18596+0315. This is similar to IRAS 18460+0151 and presents a wide component only at the WF position. The shaded area reaches from 90 to 105 km s^{-1}.

and 3 in IRAS 18460-0151 and IRAS 18596+0315, except for ^{13}CO in IRAS 18460-0151; this unusually high line ratio is due to the low velocity-integrated temperature measured in the ^{13}CO $J = 1 \rightarrow 0$ line. For IRAS 18286-0959, the CO $(2 - 1)/(1 - 0)$ ratios are 0.4 and 0.6 for the blue and red components; these values, more typical of diffuse clouds, indicate different excitation conditions in this source.

Another interesting reading of the Table 3 may be made by computing the CO/^{13}CO line ratio in IRAS 18460-0151 and IRAS 18596+0315 independently for each J transition. In all cases except for the $J = 1 \rightarrow 0$ case of IRAS 18460-0151 these ratios are extremely low, between 2.6 and 3.3. It is worth noting that Imai et al. (2012) have measured similar values in IRAS 16342-3814. This low line ratio may be interpreted in terms of high opacity of the CO line, or a real decrease of the isotopic ratio produced in specific events of the star evolution, such as the first dredge-up at the beginning of the RGB (Karakas & Lattanzio 2007), or the deep mixing at the end of the same phase (Eggleton et al. 2008). This last hypothesis, first discussed by He et al. (2008), is supported by the fact that a low

^{12}CO/^{13}CO line ratio is very common in PNe (Bujarrabal et al. 2005) and proto-PNe (Bujarrabal et al. 2001).

The question arises why CO is detected in some WFs (IRAS 18460-0151, IRAS 18596+0315, and probably IRAS 18286-0959), while in others (e.g., IRAS 16552-3050, IRAS 18113-2503, or IRAS 19134+2131) it is clearly absent. In the remaining four sources (IRAS 18043-2116, OH12.8-0.9, W43A, and IRAS 19190+1102), Galactic contamination prevents any conclusive association or non-association of CO to the WFs, because in these cases there are intense spectral components in the stellar velocity range. Unfortunately, the few detections and unambiguous non-detections preclude any statistically significant discussion, and all suggestions must needs be highly speculative. We do not see any correlation of detectability with obvious physical parameters, such as the source distance or the envelope masses (estimated by Durán-Rojas et al., in preparation). It is possible that CO is detected in WFs where the abundance of this molecule is enhanced.

To explore this possibility, we investigated the morphology of the water maser emission where high angular reso-
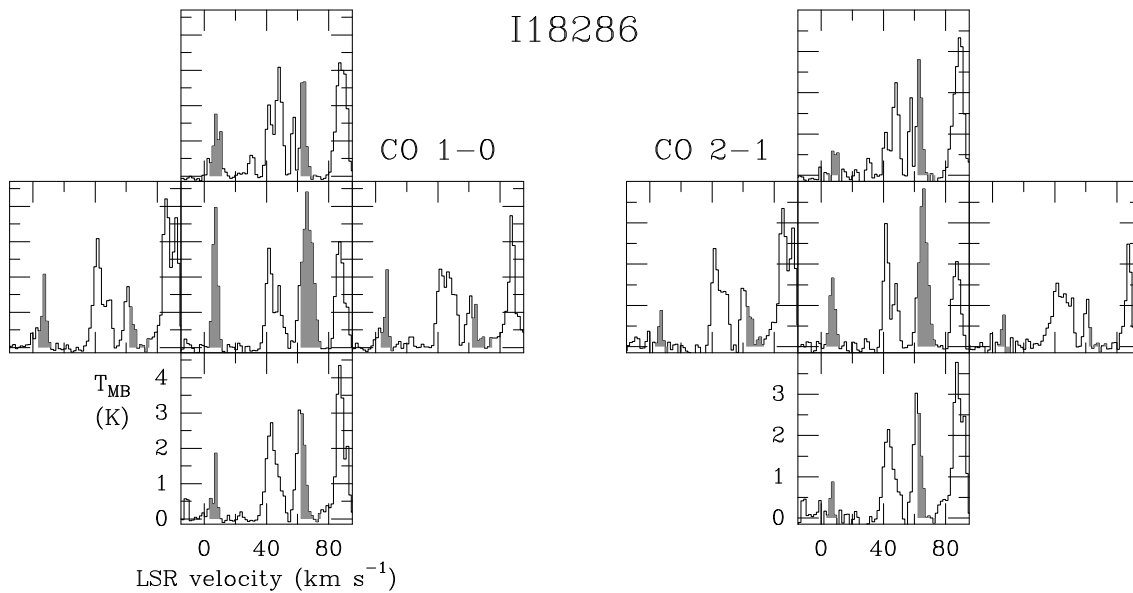
Fig. 7. Same as Figs. 5 and 6 for IRAS 18286-959. In this case, a different pattern is proposed in the CO and ^{13}CO associated with the WF. Two narrow velocity components, symmetrically located with respect to the stellar velocity, are found with a higher intensity towards the star position.

Table 3. CO and ^{13}CO parameters

SHELL FITTING

Source	Line	Area K km s^{-1}	V_{pk} km s^{-1}	V_{exp} km s^{-1}	s_τ
IRAS 18460-0151	CO 1 → 0	10.6(2.6)	127.1(3.5)	19.9(0.9)	-0.72(0.21)
IRAS 18460-0151	CO 2 → 1	21.3(1.7)	125.3(1.9)	18.3(0.6)	-0.85(0.08)
IRAS 18460-0151	^{13}CO 1 → 0	0.4(0.1)	125.0(5.1)	10.3(3.0)	1.02(0.71)
IRAS 18460-0151	^{13}CO 2 → 1	6.6(0.6)	126.3(1.4)	21.8(0.5)	-0.96(0.06)
IRAS 18596+0315	CO 1 → 0	2.2(0.4)	89.9(1.4)	16.0(1.4)	-0.95(0.17)
IRAS 18596+0315	CO 2 → 1	6.5(0.9)	87.3(1.8)	18.8(1.8)	-0.83(0.54)
IRAS 18596+0315	^{13}CO 1 → 0	0.8(0.2)	83.1(6.2)	23.9(5.1)	0.06(0.52)
IRAS 18596+0315	^{13}CO 2 → 1	2.0(0.3)	90.3(1.6)	18.3(1.5)	-0.93(0.27)

GAUSSIAN FITTING

Source	Line	Area K km s^{-1}	V_{pk} km s^{-1}	ΔV km s^{-1}	T_{pk} K
IRAS 18286-0959	CO 1 → 0 blue	12.0(0.5)	6.5(0.5)	4.6(0.4)	2.5(0.3)
IRAS 18286-0959	CO 1 → 0 red	41.2(0.6)	66.5(0.6)	7.4(0.7)	5.2(0.4)
IRAS 18286-0959	CO 2 → 1 blue	5.3(0.6)	7.5(0.5)	4.9(0.6)	1.0(0.2)
IRAS 18286-0959	CO 2 → 1 red	26.1(0.7)	65.6(0.4)	6.1(0.6)	4.0(0.3)

Notes. One-sigma errors within parenthesis.

lution was available. In the sources without a clear detection of CO emission, the water masers trace only bipolar jets, with well-separated redshifted and blueshifted components (Imai et al. 2007b; Suárez et al. 2008; Gómez et al. 2011), while in IRAS 18460-0151 there is a central maser structure tracing low-collimating mass loss. If shocks enhance CO abundance in the gas phase (due to chemical reactions or evaporation of ices), the detection of CO lines would be favoured in sources with current episodes of low-collimation mass-loss (in addition to the collimated jets), where shocked regions would occupy a large solid angle. However, the proper evaluation of this possi-
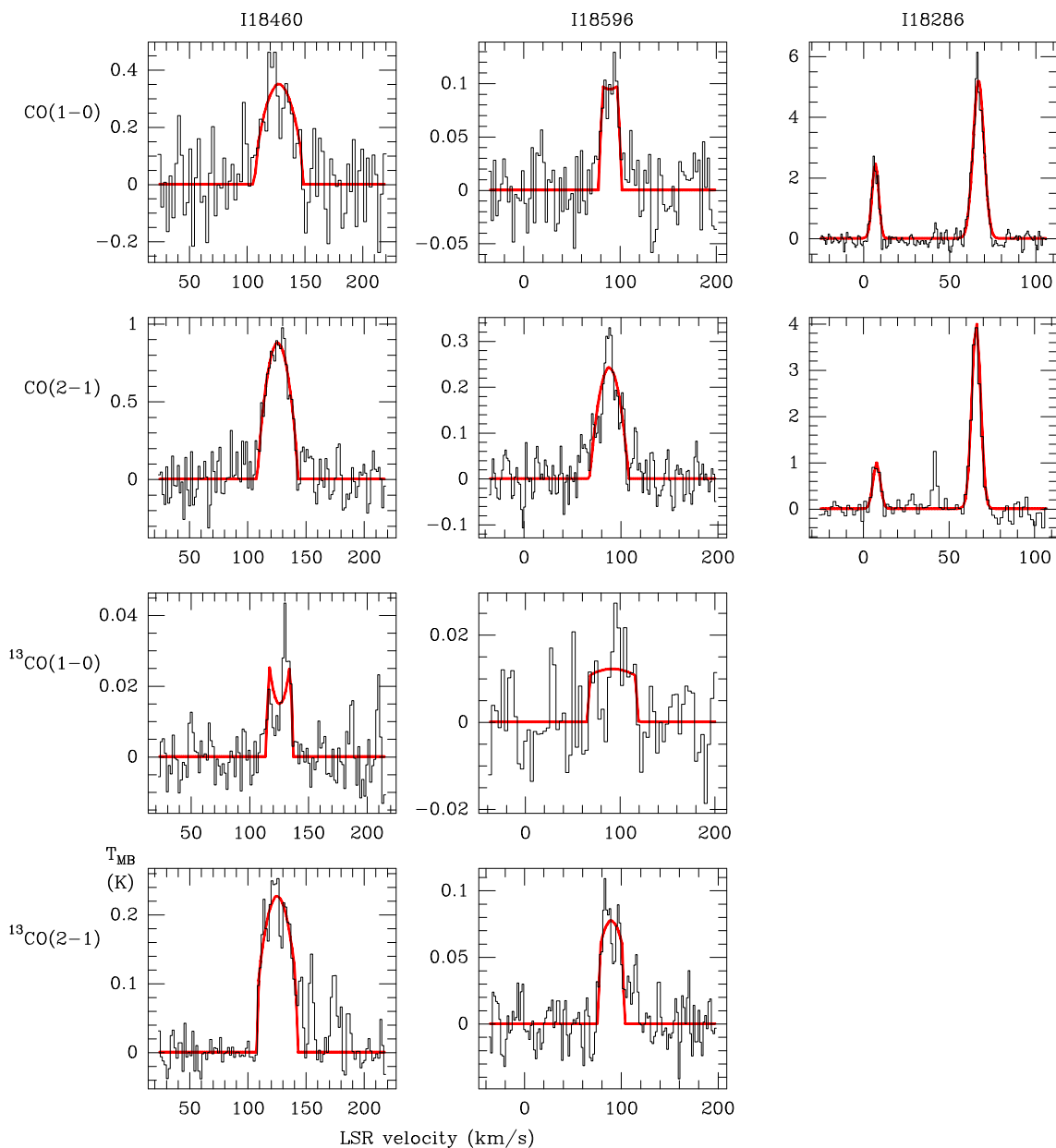
Fig. 8. Final spectra in the three cases reported as probable detections of CO and ^{13}CO gas in WFs. These spectra are the result of subtracting synthesized off-source from on-source spectra for each source and transition. The superposed red lines are fits as circumstellar shells (for IRAS 18460+0151 and IRAS 18596+0315) or Gaussian profiles (for IRAS 18286-0959). Each isotope and transition has been fitted independently (see text).

bility would require interferometric observations, to determine whether CO emission is co-located with water masers.

4.2. Physical parameters

Aiming to shed more light on the origin of the detected CO and ^{13}CO, and also to estimate the physical parameters of the envelopes, we have proceeded with non-LTE radiative modelling, using our own code of the *Large Velocity Gradient* (LVG) approach. For a given set of physical conditions –mainly the kinetic temperature T_k, H$_2$ volume density $n(H_2)$, line width and CO column density N(CO)–, this code iterates and computes the population of the rotational levels, and predicts some line intensities. More details of the LVG methodology is provided in the appendix.

The code did not provide satisfactory results for IRAS 18286-0959 for either of the two components. The low (2-1)/(1-0) line ratio that is observed could only be reproduced at $n(H_2)$ values well below 10^2 cm^{-3}, typical of interstellar clouds, and N(CO) abnormally high. Nonetheless, and regarding our observational findings and those of Imai et al. (2009), this case should not be ruled out because the CO is clearly contaminated by foreground or background Galactic emission.

For the other two sources, a summary of the best-fit results is shown in Table 4. For IRAS 18460-0151, the LVG approach does not provide any solution for T_k above 50 K. For T_k=10 K the solutions are optically thick, and for the range 20–50 K the line emission is optically thin (or moderately thick for T_k=20 K). The case of IRAS 18596+0315, for a distance of 4.6 kpc, is remarkably similar to IRAS 18460-0151. In both cases, the total

envelope masses are between ~ 0.2 and 0.4 $M_\odot$, the mean densities around 10^4 cm^{-3}, and the mass-loss rates of the order of 10^{-4} $M_\odot$ yr^{-1}. The CO emission in IRAS 18596+0315 is more opaque than in IRAS 18460-0151. The ^{12}C/^{13}C ratio –computed as the ratio between the column densities of ^{12}CO and ^{13}CO– is low in both cases, although in IRAS 18460-0151 it is not exceptionally low.

The line profiles (Fig. 8) and their corresponding shell fitting (Table 3) show that the envelope is characterized by moderate opacities. Taking this into account, the lower values of T_k should be favoured. Another strong argument that favours low T_k is provided after comparing the CO opacities of different transitions; the (2-1)/(1-0) opacity ratios are unacceptably high for the highest T_k, because they exceed the observed line ratios by far. The low values of T_k are consistent with a scenario in which CO arises from the outer parts of the envelope.

Low temperatures also characterize the CO emission in most of the known post-AGB stars (Bujarrabal et al. 2001, and references therein). Furthermore, the values of the mass envelopes and the mass-loss rates agree very well with those derived previously (Knapp & Morris 1985; Bujarrabal et al. 2001, 2005; De Beck et al. 2010). The high mass-loss rates derived from the LVG fitting are compatible with the mass-loss experienced by the AGB stars with the highest masses (Bloecker 1995). Thus, the original masses of these sources are estimated to be in the range of 4–8 $M_\odot$.

The resulting parameters derived for the far kinematic distance of IRAS 18596+0315 (8.8 kpc) is, however, dramatically different with respect to the others. Firstly, the range of possible values of T_k is more restrictive, in the range 30–50 K. Secondly, due to a higher N(CO), the mass grows to 2 $M_\odot$, n(H$_2$) is close to 10^5 cm^{-3}, and the mass-loss rate is of the order of 10^{-3} $M_\odot$ yr^{-1}. This case is indeed puzzling. The envelope mass is very large (although compatible with that obtained by Durán-Rojas et al., in preparation), and the mass-loss rate reaches a value that is too high within current models (Bloecker 1995), and has not been observed in evolved stars with a low- and intermediate-mass progenitor. Unless something really unique occurs in this source, this result favour the nearest kinematic distance for this source, around 4.6 kpc.

Finally, a word of caution is given with respect to the LVG estimates. We made strong assumptions about the size of the envelope and CO abundance. These assumptions and the uncertainty of the distances may produce variations of the parameters of a factor of two or even larger. The structure of CSEs in WFs is indeed more complex, due to the presence of shocks, bipolar outflows, or episodic mass-loss events. The complex heating and cooling processes due to excitation of molecules contribute to its complexity.

5. Conclusions

From this survey, we have discovered CO emission associated with two new WF sources: IRAS 18460-0151 and IRAS 18596+0315. A third case, IRAS 18286-0959, is reported as tentative. These CO detections in WFs add new cases to IRAS 16342-3814, the only one previously known (He et al. 2008), and are the most promising candidates in which to study the molecular gas around WFs.

The wide component found in IRAS 18460-0151 was interpreted as the envelope of the former AGB stage. By non-LTE radiative modelling, we computed some physical parameters. The total envelope masses are around 0.2 $M_\odot$, the mass-loss rates are

of the order of 10^{-4} $M_\odot$ yr^{-1}, and the CO emission is moderately thick. The kinetic temperatures derived are rather low, in the range from 10 K to 50 K. Taking into account the moderate opacities derived from the line profiles, we favour the low values of T_k, which is also consistent with a scenario where the CO arises from the cold, outer parts of the envelopes.

For IRAS 18596+0315 we also discovered a wide velocity component. For the near kinematic distance (4.6 kpc), the LVG results were similar to those of IRAS 18460-0151. For the far kinematic distance (8.8 kpc), however, we predict higher kinetic temperatures (30–50 K), large envelope masses ($\simeq$ 2 $M_\odot$), and mass-loss rates one order of magnitude higher. These last values are hard to explain with the usual parameters found in other AGB envelopes, or with theoretical considerations (Bloecker 1995).

For IRAS 18286-0959, we found two narrow velocity components, symmetrically located with respect to the stellar velocity, ~ 30 km s^{-1} apart. Previous observations of the same source at the $J = 3 \rightarrow 2$ transition (Imai et al. 2009) failed to detect these components, but reported another narrow component close to the stellar velocity. Line contamination by Galactic background affects the computation of parameters and prevents further conclusions. Nonetheless, it is possible that the CO detected arises from somewhere in the jets traced by the water maser at 22 GHz, and this case deserve a more detailed analysis in the future. We speculate whether CO is detected in WFs in which low-collimated mass-loss enhances the CO abundance in a relatively large area of the envelope.

The detection and study of circumstellar envelopes around WFs are the key to understanding how the mass ejections took place during the last stages of evolution of these objects. The high mass-loss rates derived from our CO data indicate that we are seeing the mass ejected at the end of the AGB phase, and that these objects derive from relatively massive (4–8 $M_\odot$) progenitors. Sensitive, high-resolution observations are the natural follow-up of this work, and they may show how mass is ejected at the very end of the AGB phase, and its influence in shaping multipolar planetary nebulae.

References

Baud, B., Sargent, A. I., Werner, M. W., & Bentley, A. F. 1985, ApJ, 292, 628
Bloecker, T. 1995, A&A, 297, 727
Boboltz, D. A., & Marvel, K. B. 2005, ApJ, 627, L45
Boboltz, D. A., & Marvel, K. B. 2007, ApJ, 665, 680
Bujarrabal, V., Castro-Carrizo, A., Alcolea, J., & Neri, R. 2005, A&A, 441, 1031
Bujarrabal, V., Castro-Carrizo, A., Alcolea, J., & Sánchez Contreras, C. 2001, A&A, 377, 868
Bujarrabal, V., & Cernicharo, J. 1994, A&A, 288, 551
Day, F. M., Pihlstrom, Y. M., Claussen, M. J., & Sahai, R. 2010, ApJ, 713, 986
Deacon, R. M., Chapman, J. M., Green, A. J., & Sevenster, M. N. 2007, ApJ, 658, 1096
De Beck, E., Decin, L., de Koter, A., et al. 2010, A&A, 523, A18
Deguchi, S., Nakashima, J.-i., Kwok, S., & Koning, N. 2007, ApJ, 664, 1130
Diamond, P. J., Norris, R. P., Rowland, P. R., Booth, R. S., & Nyman, L.-A. 1985, MNRAS, 212, 1
Dijkstra, C., Waters, L. B. F. M., Kemper, F., et al. 2003, A&A, 399, 1037
Eggleton, P. P., Dearborn, D. S. P., & Lattanzio, J. C. 2008, ApJ, 677, 581
Engels, D., & Jiménez-Esteban, F. 2007, A&A, 475, 941
Engels, D., Schmid-Burgk, J., & Walmsley, C. M. 1986, A&A, 167, 129

Table 4. Results from the LVG modelling of IRAS 18460-0151 and IRAS 18596+0315

MASS-RELATED PARAMETERS

Source	T_k	N(CO)	mass	n(H$_2$)	V_{exp}	$\dot{M}$	^{12}C/^{13}C
	K	$10^{17}\,\mathrm{cm}^{-2}$	M$_\odot$	$10^3\,\mathrm{cm}^{-3}$	km s^{-1}	M$_\odot$ yr^{-1}	
IRAS 18460-0151	10	1.57(0.44)	0.20	7.85(2.4)	20.1	2.6 10^{-4}	30
IRAS 18460-0151	20–50	1.50(0.32)	0.19	7.50(2.1)	20.1	2.5 10^{-4}	23
IRAS 18596+0315[a]	10	2.70(0.83)	0.35	13.5(4.1)	17.8	3.9 10^{-4}	9
IRAS 18596+0315[a]	20–50	1.91(0.26)	0.25	9.55(2.3)	17.8	2.8 10^{-4}	7
IRAS 18596+0315[b]	30–50	18.0(4.8)	2.32	90.0(23)	17.8	2.6 10^{-3}	13

OPACITIES

Source	T_k (K)	CO 1–0	CO 2–1	^{13}CO 1–0	^{13}CO 2–1
IRAS 18460-0151	10	0.82(0.46)	1.65(0.70)	0.04(0.02)	0.09(0.03)
IRAS 18460-0151	20	0.23(0.10)	0.90(0.60)	0.01(0.01)	0.06(0.04)
IRAS 18460-0151	30	0.09(0.04)	0.62(0.30)	optically thin	
IRAS 18460-0151	40	0.04(0.02)	0.45(0.25)	optically thin	
IRAS 18460-0151	50	0.01(0.01)	0.37(0.21)	optically thin	
IRAS 18596+0315[a]	10	1.47(0.60)	2.66(1.20)	0.20(0.09)	0.43(0.18)
IRAS 18596+0315[a]	20	0.04(0.02)	1.10(0.40)	0.04(0.03)	0.21(0.14)
IRAS 18596+0315[a]	30	0.02(0.01)	0.73(0.40)	0.02(0.01)	0.14(0.12)
IRAS 18596+0315[a]	40	optically thin			
IRAS 18596+0315[a]	50	optically thin			
IRAS 18596+0315[b]	30	0.97(0.40)	2.90(1.20)	0.10(0.03)	0.32(0.07)
IRAS 18596+0315[b]	40	0.63(0.35)	2.12(0.70)	0.06(0.02)	0.22(0.09)
IRAS 18596+0315[b]	50	0.38(0.20)	1.40(0.50)	0.04(0.01)	0.14(0.07)

Notes. CO abundance of 10^{-4} assumed. Distances from Table 1. One-sigma errors within parenthesis.
[a] Assumed distance is 4.6 kpc.
[b] Assumed distance is 8.8 kpc.

García-Segura, G., López, J. A., & Franco, J. 2005, ApJ, 618, 919

Gómez, J. F., Rizzo, J. R., Suárez, O., Miranda, L. F., Guerrero, M. A., Ramos-Larios, G. 2011, ApJL, 739, L14

Gómez, Y., Rodríguez, L. F., Contreras, M. E., & Moran, J. M. 1994, Rev. Mexicana Astron. Astrofis., 28, 97

Green, S., & Thaddeus, P. 1976, ApJ, 205, 766

He, J. H., Imai, H., Hasegawa, T. I., Campbell, S. W., & Nakashima, J. 2008, A&A, 488, L21

Imai, H., Nakashima, J.-i., Diamond, P. J., Miyazaki, A., & Deguchi, S. 2005, ApJ, 622, L125

Imai, H. 2007, IAU Symposium, 242, 279

Imai, H., Sahai, R., & Morris, M. 2007, ApJ, 669, 424

Imai, H., He, J.-H., Nakashima, J.-I. U., Nobuharu, Deguchi, S., & Koning, N. 2009, PASJ, 61, 1365

Imai, H., Chong, S. N., He, J.-H., et al. 2012, PASJ, 64, 98

Imai, H., Kurayama, T., Honma, M., & Miyaji, T. 2013a, PASJ, 65, 28

Imai, H., Deguchi, S., Nakashima, J.-i., Kwok, S., & Diamond, P. J. 2013b, ApJ, 773, 182

Jacoby, G. H., Kronberger, M., Patchick, D., et al. 2010, PASA, 27, 156

Karakas, A., & Lattanzio, J. C. 2007, PASA, 24, 103

Knapp, G. R., & Morris, M. 1985, ApJ, 292, 640

Likkel, L., & Morris, M. 1988, ApJ, 329, 914

Mauersberger, R., Guelin, M., Martin-Pintado, J., et al. 1989, A&AS, 79, 217

Neri, R., Kahane, C., Lucas, R., Bujarrabal, V., & Loup, C. 1998, A&AS, 130, 1

Reid, M. J., Menten, K. M., Zheng, X. W., et al. 2009, ApJ, 700, 137

Sahai, R., & Trauger, J. T. 1998, AJ, 116, 1357

Sakamoto, S., Hasegawa, T., Hayashi, M., Handa, T., & Oka, T. 1995, ApJS, 100, 125

Sevenster, M. N., Chapman, J. M., Habing, H. J., Killeen, N. E. B., & Lindqvist, M. 1997, A&AS, 122, 79

Sobolev, V. V. 1960, Moving envelopes of stars (Harvard University Press, Cambridge)

Soker, N. 1998, ApJ, 496, 833

Suárez, O., Gómez, J. F., & Miranda, L. F. 2008, ApJ, 689, 430

Suárez, O., Gómez, J. F., Miranda, L. F., Torrelles, J. M., Gómez, Y., Anglada, G., & Morata, O. 2009, A&A, 505, 217

Suárez, O., Gómez, J. F., & Morata, O. 2007, A&A, 467, 1085

te Lintel Hekkert, P., Versteege-Hensel, H. A., Habing, H. J., & Wiertz, M. 1989, A&AS, 78, 399

Teyssier, D., Hernandez, R., Bujarrabal, V., Yoshida, H., & Phillips, T. G. 2006, A&A, 450, 167

van der Tak, F. F. S., Black, J. H., Schöier, F. L., Jansen, D. J., & van Dishoeck, E. F. 2007, A&A, 468, 627

Yamamura, I., Onaka, T., Kamijo, F., Izumiura, H., & Deguchi, S. 1993, PASJ, 45, 573

Yung, B. H. K., Nakashima, J.-i., Imai, H., et al. 2011, ApJ, 741, 94

Appendix A: LVG modelling

The LVG approach is a method that solves for different geometries the radiative transfer equations and the level populations iteratively and without assuming local thermodynamical equilibrium. It is based on the escape probability method first introduced by Sobolev (1960). This methodology has been and is widely used for determining the physical parameters of regions observed through their molecular rotational lines. An increasingly popular online version of this method is RADEX (van der Tak et al. 2007), which we also used in this work for cross-checking.

The methodology consists of decoupling the radiative transfer from the level population trough introducing a parameter β that measures the probability of a photon to escape the cloud. For an uniform sphere, it is computed by

$$\beta = (1 - e^{-\tau})/\tau, \tag{A.1}$$

where τ is the optical depth of a given transition. For an optically thin cloud, $\tau \to 0$ and therefore $\beta \to 1$, and all the photons escape the cloud. In contrast, β becomes lower for an optically thick cloud, with a limit value of zero.

We modelled a uniform spherical cloud with an arbitrary radius $r_{out} = 10^4$ AU, typical of AGB envelopes. A sphere of this size, located at the distances quoted in Table 1, would subtend at most some arcsec in the sky at the observed frequencies; therefore, we ran the code for a single point that concentrated all the emission from the envelope. The crude geometry that we had to introduce is, however, sufficient to provide first-order estimates of some global parameters, and is useful to constrain the theoretical models under development (Durán-Rojas et al., in preparation).

We corrected the observed line intensities by the beam-filling factor (which is different for each source and frequency). A CO abundance with respect to H_2 (X_{CO}) of 10^{-4} and a H_2 mass abundance of 90% were assumed. The collision partners are H_2 and He, and the collisional coefficients used were taken from Green & Thaddeus (1976). We note that, although reasonable, these assumptions certainly constitute an oversimplification and would translate into significant uncertainties in our results. The uncertainties quoted in Table 4 (one-sigma) for $N(CO)$ and $n(H_2)$ are the result of the LVG model, considering only the uncertainties in the fitting (Table 3). For the total mass and the mass-loss rate, the uncertainties were computed by the standard formulae of propagation errors.

We ran the LVG code independently for the CO and ^{13}CO species and for different values of T_k (from 10 K to 100 K, in steps of 10 K). For each temperature, we computed the radiative transfer for a grid of $n(H_2)$ and $N(CO)$, trying to find the best fit to the observed line intensities and the (2-1)/(1-0) line ratios. After determining the column densities, the opacities and envelope masses were obtained. Fig. A.1 shows an example of the fitting, where the contours represent the observed $J = 1 \to 0$ line intensity and the (2-1)/(1-0) line ratio; the position where the two sets of contours intersect determines the most probable value of $N(CO)$ and $n(H_2)$ for this value of T_k. The uncertainties in $N(CO)$ and $n(H_2)$ are also obtained from this fitting.

For IRAS 18596+0315, the procedure was applied twice, once for each of the possible kinematic distances (Table 1); for IRAS 18286-0959, we also ran the code twice, once for each velocity component.
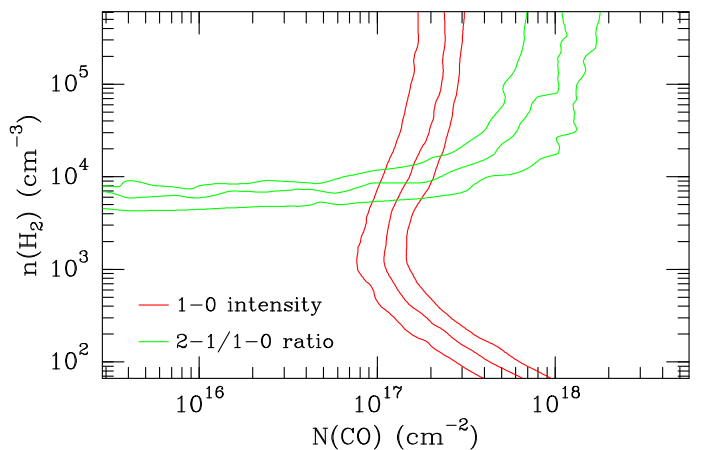
Fig. A.1. Example of the fitting using the LVG approach. The contours correspond to the observed values of the $J = 1 \to 0$ line intensity (red) and the (2-1)/(1-0) line ratio (green), together with their corresponding errors.

The mass was computed by integrating $N(CO)$ over the projected disk:

$$M = 1.1 \, (2 \, m_H) \, X_{CO}^{-1} \, [\pi \, r_{out}^2 \, N(CO)], \tag{A.2}$$

where m_H is the mass of the hydrogen atom, and the factor 1.1 accounts for the mentioned H_2 mass abundance.

Finally, the mass-loss rate was computed directly from the derived $n(H_2)$, with the only assumption of a stationary mass loss, and following the equation of continuity:

$$\dot{M} = 4 \, \pi \, r_{out}^2 \, V_{exp} \, [1.1 \, n(H_2)], \tag{A.3}$$

We remark that the mass-loss rate computed here is not the current mass-loss of the sources (that are probably in the post-AGB phase), but are the mass lost in the former AGB phase, during which the envelope was expelled.